Supplementary Information

In situ training of an in-sensor artificial neural network based on ferroelectric photosensors

Haipeng Lin[1,5], Jiali Ou[1,5], Zhen Fan[1*], Xiaobing Yan[2*], Wenjie Hu[1], Boyuan Cui[1], Jikang Xu[2], Wenjie Li[1], Zhiwei Chen[1], Biao Yang[2], Kui Liu[1], Linyuan Mo[1], Meixia Li[1], Xubing Lu[1], Guofu Zhou[3], Xingsen Gao[1] & Jun-Ming Liu[1,4]

[1]Institute for Advanced Materials and Guangdong Provincial Key Laboratory of Optical Information Materials and Technology, South China Academy of Advanced Optoelectronics, South China Normal University, 510006 Guangzhou, China.[2]Key [2]Laboratory of Brain-Like Neuromorphic Devices and Systems of Hebei Province, Hebei Key Laboratory of Photo-Electricity Information and Materials, Hebei University, 071002 Baoding, China

[3]National Center for International Research on Green Optoelectronics, South China Normal University, 510006 Guangzhou, China.

[4]Laboratory of Solid State Microstructures and Innovation Center of Advanced Microstructures, Nanjing University, 210093 Nanjing, China.

[5]These authors contributed equally: Haipeng Lin and Jiali Ou.

[*]Email: fanzhen@m.scnu.edu.cn and yanxiaobing@ime.ac.cn

This Supplementary Information file includes:

Supplementary Figures S1-S17

Supplementary Table S1

Supplementary References

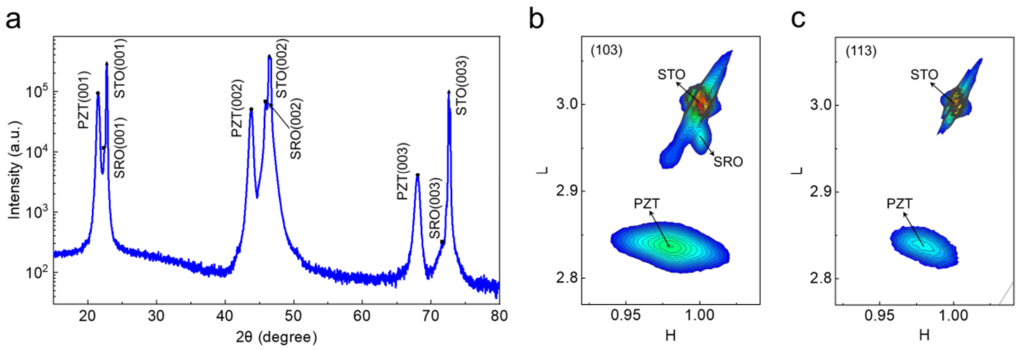

Figure S1. (a) XRD θ-2θ scan, RSMs around STO (b) (103) and (c) (113) reflections.

Figure S1a shows the presence of only the (00*l*) peaks from PZT, SRO and STO, confirming the phase purity. Figures S1b,c show that both the (103) and (113) reflections of PZT form single diffraction spots, indicating that the PZT film is epitaxially grown on the SRO-buffered STO substrate. Note that no diffraction spot from SRO is observed in Fig. S2c due to the extinction.

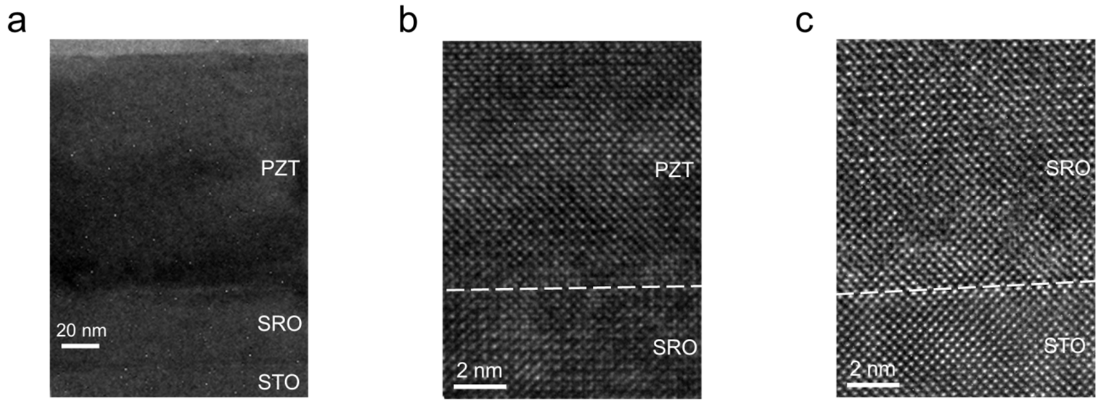

Figure S2. (a) low-magnification TEM image of the PZT/SRO/STO heterostructure, and (b,c) high-magnification TEM images around (b) PZT/SRO and (c) SRO/STO interfaces.

Figure S2a presents that the PZT/SRO/STO heterostructure with clear interfaces is established. Figures S2b,c further show that the PZT and SRO lattices are well aligned, which confirms the epitaxial growth of both the PZT and SRO layers.

The combined XRD and TEM results (Figs. S1 and S2) indicate that the PZT film exhibits a tetragonal phase with out-of-plane and in-plane lattice constants of ~4.125 and ~3.985 Å, respectively.

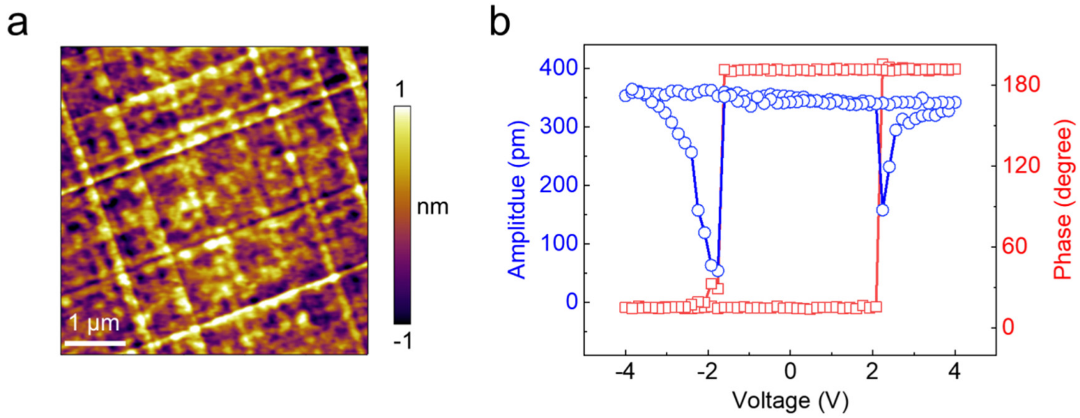

Figure S3. (a) AFM topography image and (b) PFM amplitude and phase hysteresis loops for the PZT film.

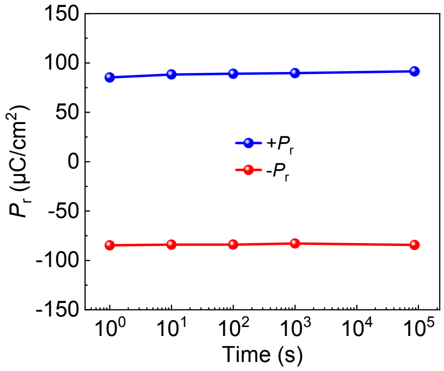

Figure S4. Polarization retention behavior of the FE-PS. Here, $+P_r$ and $–P_r$ correspond to the P_{down} and P_{up} states, respectively.

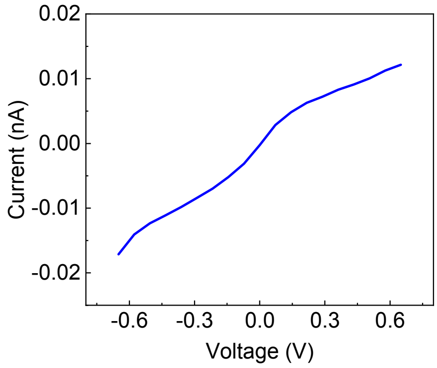

Figure S5. Dark *I*–*V* characteristics of the FE-PS.

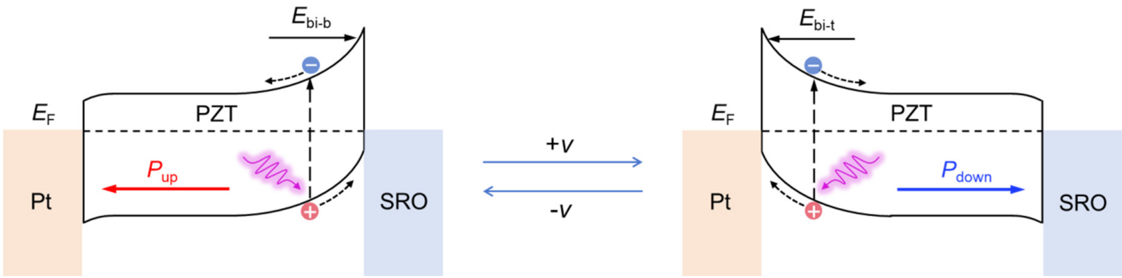

Figure S6. Schematics illustrating the operation mechanism of the Pt/PZT/SRO FE-PS, i.e., the polarization control of photoresponse via the Schottky barrier modulation.

In our previous work[1], through comprehensive investigations on the ferroelectric, dielectric, conduction, and photovoltaic behaviors of the Pt/PZT/SRO FF-PS, we demonstrated that the switchable photovoltaic behavior in this device could be attributed to the polarization-modulated Schottky barrier. In brief, the polarization of PZT can significantly modify the barrier heights at the top and bottom interfaces as well as the associated built-in fields (E_{bi-t} and E_{bi-b}, respectively). In the full P_{up} state, the negative and positive polarization charges are present at the PZT/SRO and Pt/PZT interfaces, respectively. Due to these polarization charges, the bottom barrier height and E_{bi-b} are enhanced, while the top barrier height and E_{bi-t} are reduced (or even eliminated) (see the left panel of Fig. S6). The downward E_{bi-b} therefore dominates and generates an overall positive photocurrent. By contrast, the E_{bi-t} dominates in the full P_{down} state, producing an overall negative photocurrent (see the right panel of Fig. S6). In the intermediate polarization states, the relative proportion of upward and downward domains may determine the magnitude and direction of overall photocurrent, and hence multilevel photocurrents are accessible.

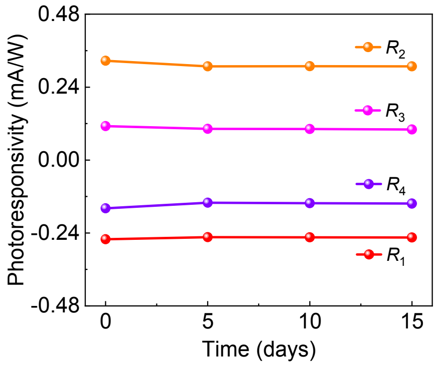

Figure S7. Long-term retention of photoresponsivity for the FE-PS. The 4 different photoresponsivities correspond to the trained weights in the experiment of in situ training (see Fig. 5e in the main text).

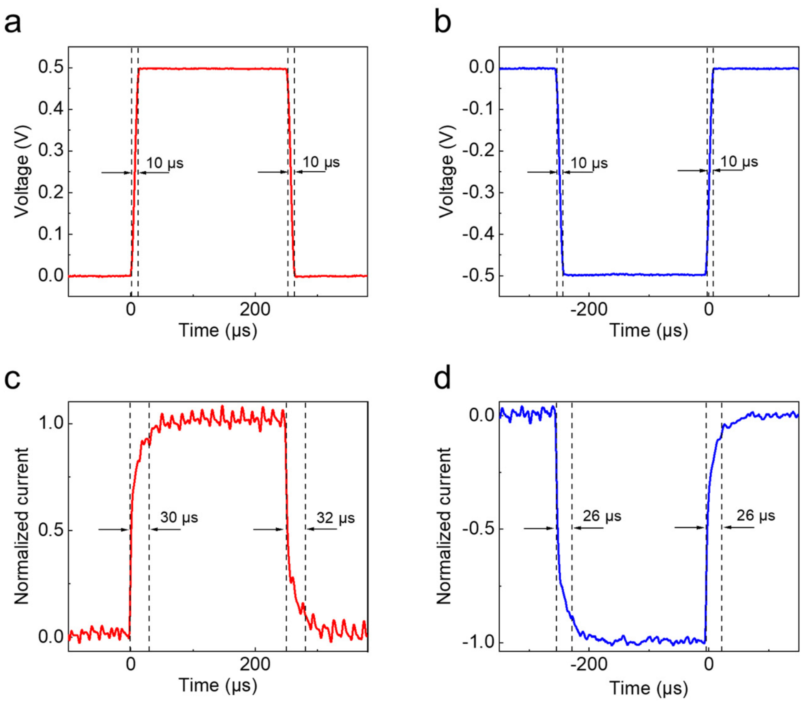

Figure S8. Waveforms of (a) +0.5 V/250 μs (b) –0.5 V/250 μs pulses directly measured with an oscilloscope. Transient current responses of a 50 MΩ resistor to (c) +0.5 V/250 μs (d) –0.5 V/250 μs pulses, measured with the amplifying circuit same as that used in the transient photoresponse measurement for the FE-PS.

To demonstrate that the measured photoresponse times of the FE-PS are limited by the amplifying circuit, the FE-PS is replaced by a 50 MΩ resistor, and its current responses to voltage pulses are measured with the same amplifying circuit. The amplitude of the applied voltage pulses is designed to be 0.5 V, allowing the resistor to generate a 10 nA current that is similar to in magnitude to the photocurrent produced by the FE-PS. In addition, the 10%–90% rising and falling times of the applied voltage pulses are designed to be 10 μs (Figs. S8a,b), which are similar to those of the light signals.

In the ideal case, the current response of the resistor would follow the waveform of the applied voltage pulse (Figs. S8a,b). However, as shown in Figs. S8c,d, the 10%–90% current rising and falling times measured with the amplifying circuit are both approximately 30 μs, close to those of the FE-PS. These results suggest that the measured response times are limited by the amplifying circuit.

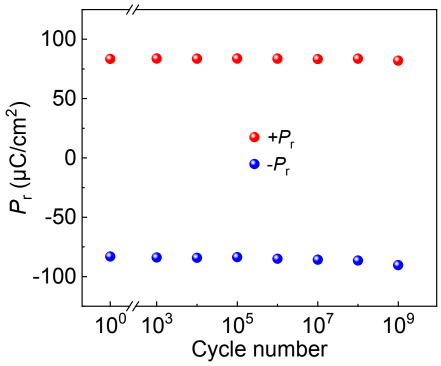

Figure S9. Polarizations as a function of endurance cycle. Here, $+P_r$ and $-P_r$ correspond to the P_{down} and P_{up} states, respectively, and ±3.5 V/0.5 μs pulses are used to switch the device cyclically.

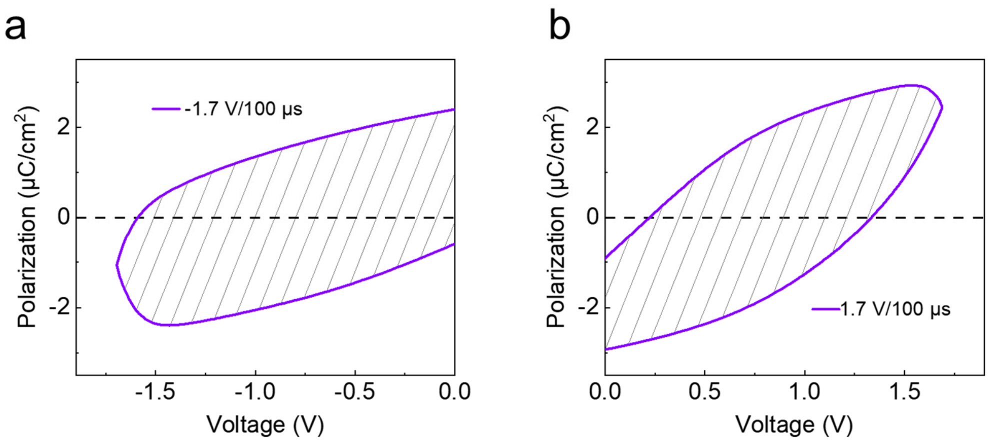

Figure S10. Typical monopolar *P-V* hysteresis loops measured with (a) –1.7 V/100 μs and (b) +1.7 V/100 μs pulses.

To measure the energy consumption of the FE-PS, the method reported in Ref. [2] is used. In brief, the monopolar *P-V* loop is measured, and then the energy consumption can be obtained by multiplying the shaded area of the *P-V* loop (see Figs. S10a,b) and the device area. Using this method, the energy consumptions of the FE-PS are measured to be ~1.68 nJ and ~1.85 nJ, for the –1.7 V/100 μs and +1.7 V/100 μs pulses respectively, giving rise to an average energy consumption of ~1.77 nJ. Note that the –1.7 V/100 μs and +1.7 V/100 μs pulses are able to tune the photoresponsivity (results not shown).

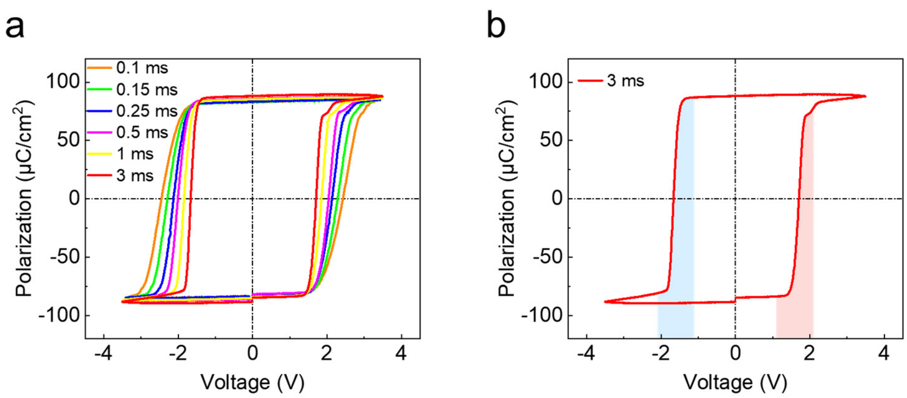

Figure S11. (a) Bipolar *P-V* hysteresis loops measured with different pulse widths. (b) *P-V* loop at the pulse width of 3 ms along with the colored regions indicating the ranges of the applied pulse voltages in the LTP/LTD measurement.

Figure S11a shows that the coercive voltage decreases with increasing pulse width, which is a typical feature of ferroelectric devices[3]. In the LTP/LTD measurement, a pulse width of 3 ms is used. At this pulse width, the coercive voltages are ~±1.70 V. It is seen from Fig. S11b that the applied pulse voltages in the LTP/LTD measurement are around the coercive voltages.

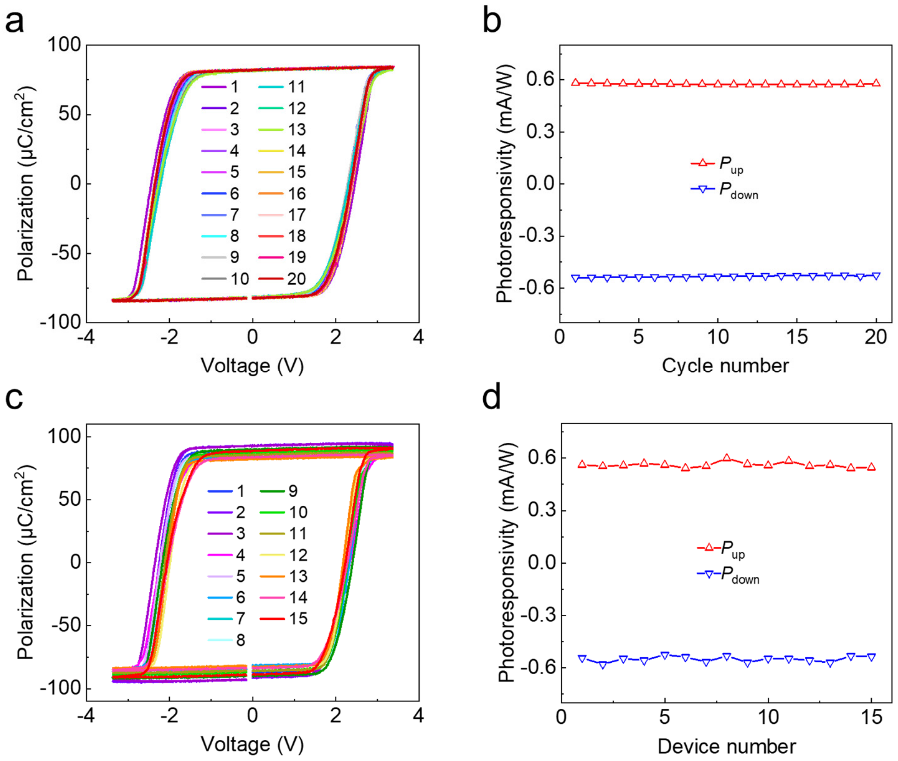

Figure S12. (a,c) Bipolar *P-V* hysteresis loops and (b,d) photocurrents in the full P_{up} and P_{down} states measured for (a,b) 20 cycles and (c,d) 15 different FE-PSs.

It is seen from Fig. S12 that both the polarization and photocurrent show little changes across different measurement cycles and devices. Based on the photocurrent data in Figs. S12b,d, the C2C and D2D variations of the FE-PS are calculated to be ~0.66% and ~2.72%, respectively.

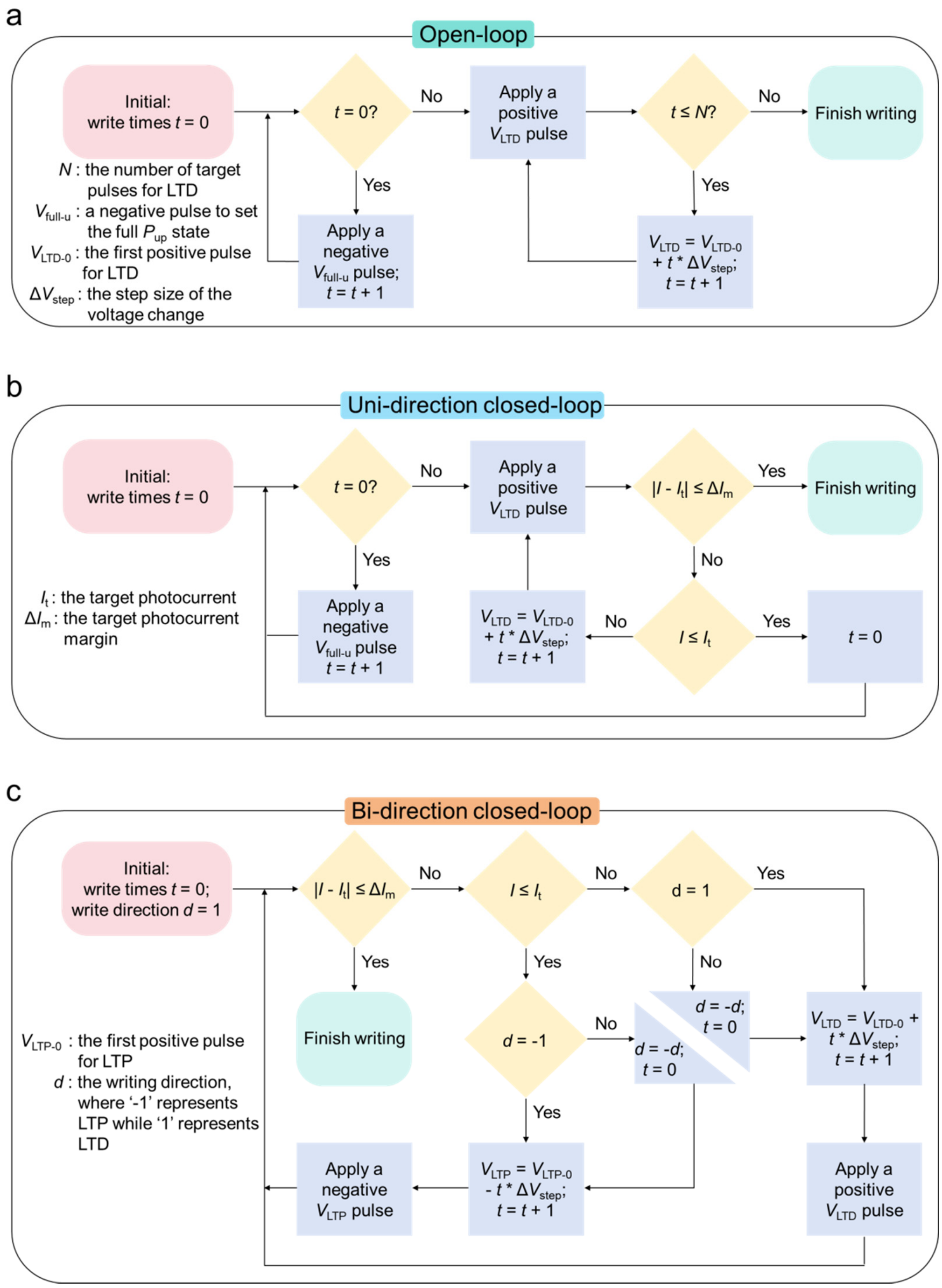

Figure S13. Flowcharts of (a) open-loop, (b) uni-directional closed-loop, and (c) bi-directional closed-loop programming schemes.

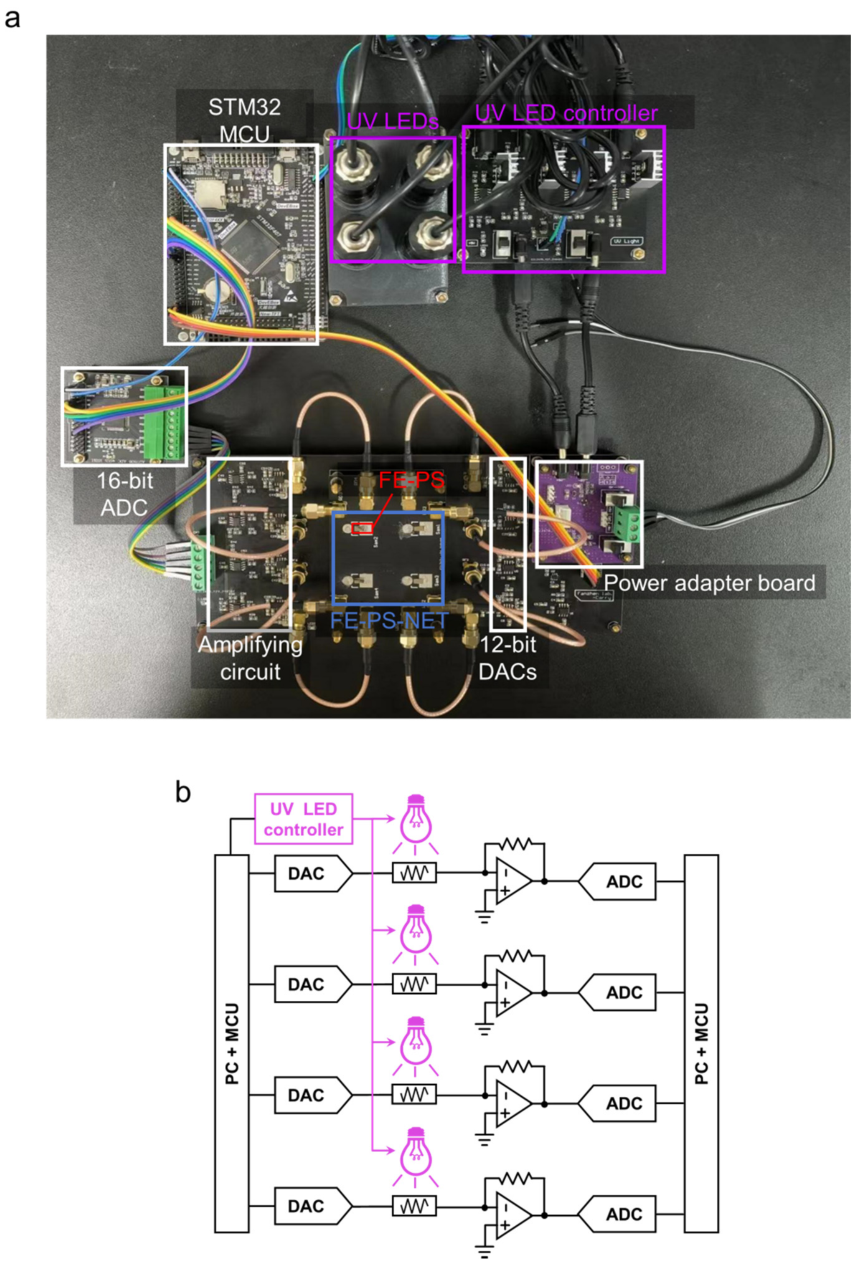

Figure S14. (a) Photograph and (b) schematic circuit diagram of the hardware platform for implementing various programming schemes.

This hardware platform is also used for the in situ training of the FE-PS-NET to recognize traffic signs. After any training epoch, the FE-PS-NET can be conveniently transferred to the circuit of the vehicle (see Fig. S15) for the test.

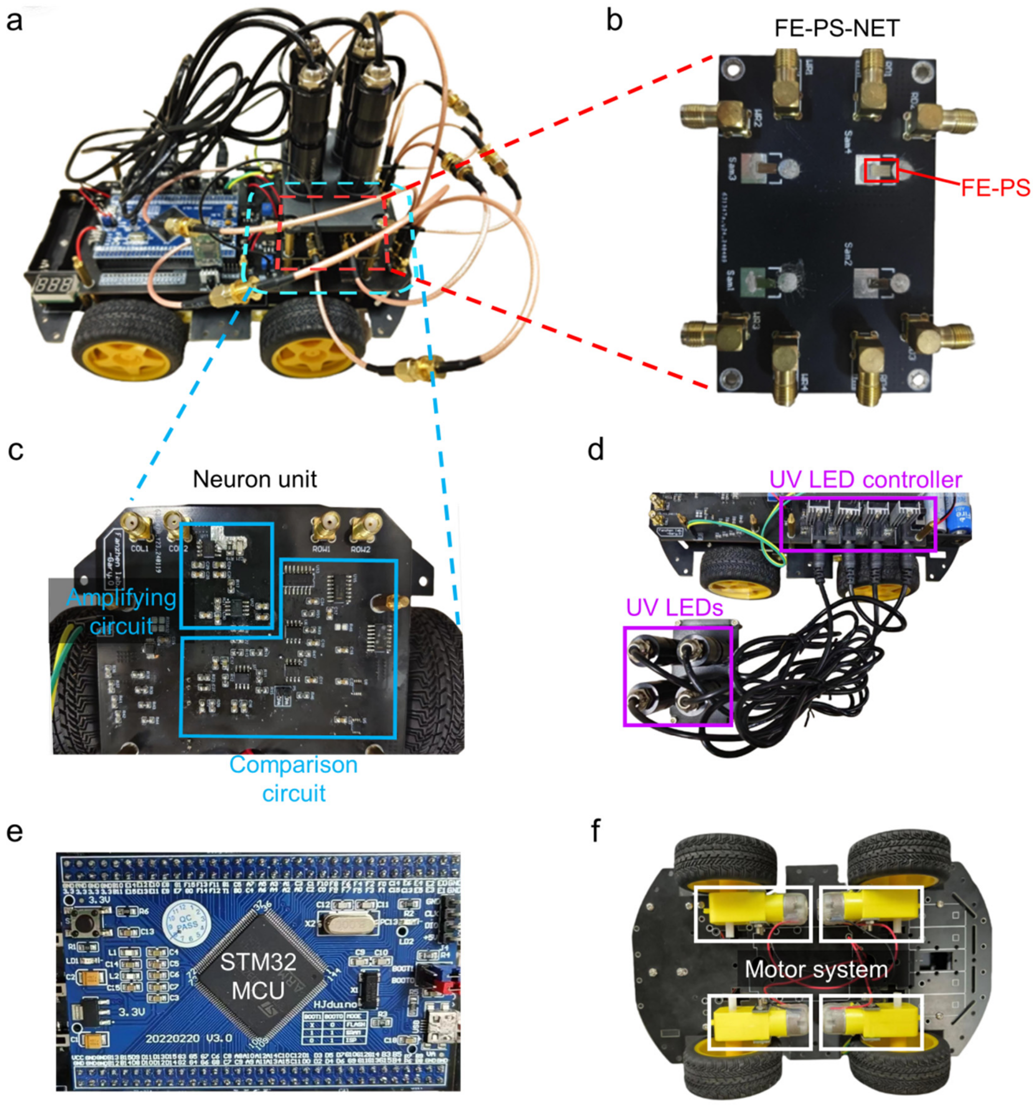

Figure S15. Photographs of (a) the whole vehicle, (b) FE-PS-NET comprising 4 FE-PSs, (c) neuron unit comprising amplifying circuit and comparison circuit, (d) UV LEDs and their controller, (e) STM32 MCU, and (f) motor system.

In the demonstration of the navigation of the vehicle based on the real-time recognition result from the FE-PS-NET, the output current of the FE-PS-NET is fed to the neuron unit, and then sent to the motor system of the vehicle to control its movements. The STM32 MCU is used only for controlling LEDs to generate the traffic signs.

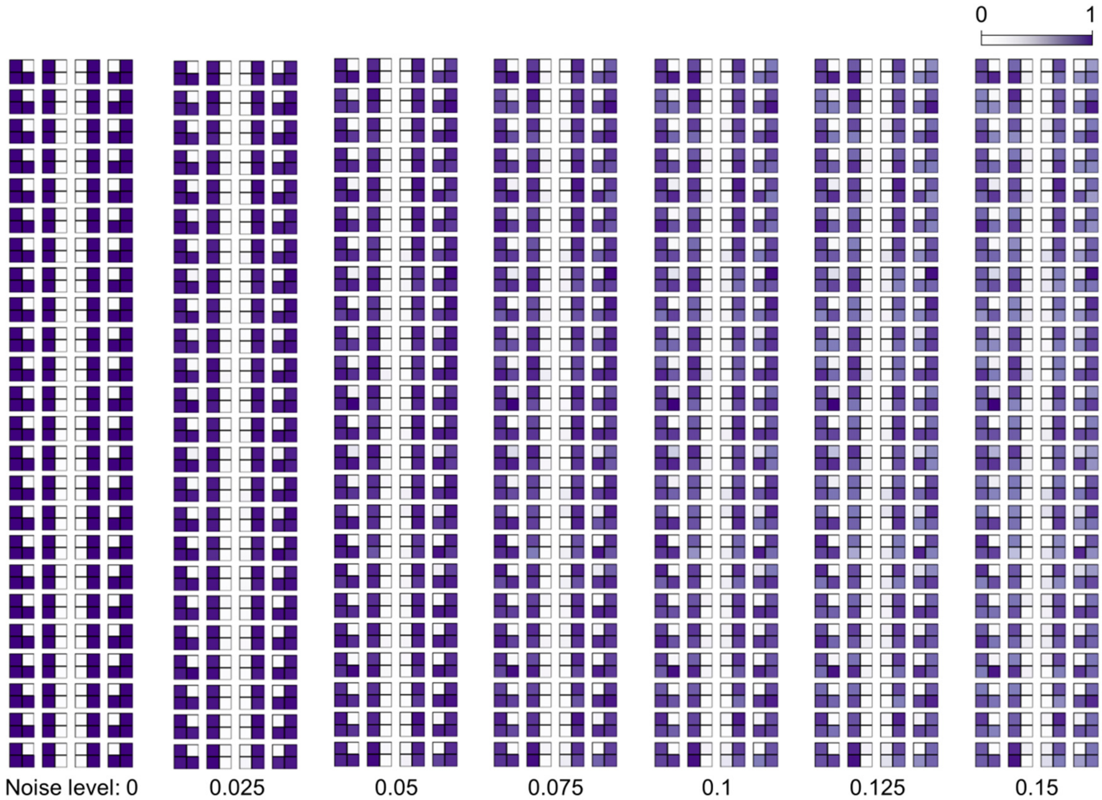

Figure S16. Test traffic signs with different noise levels.

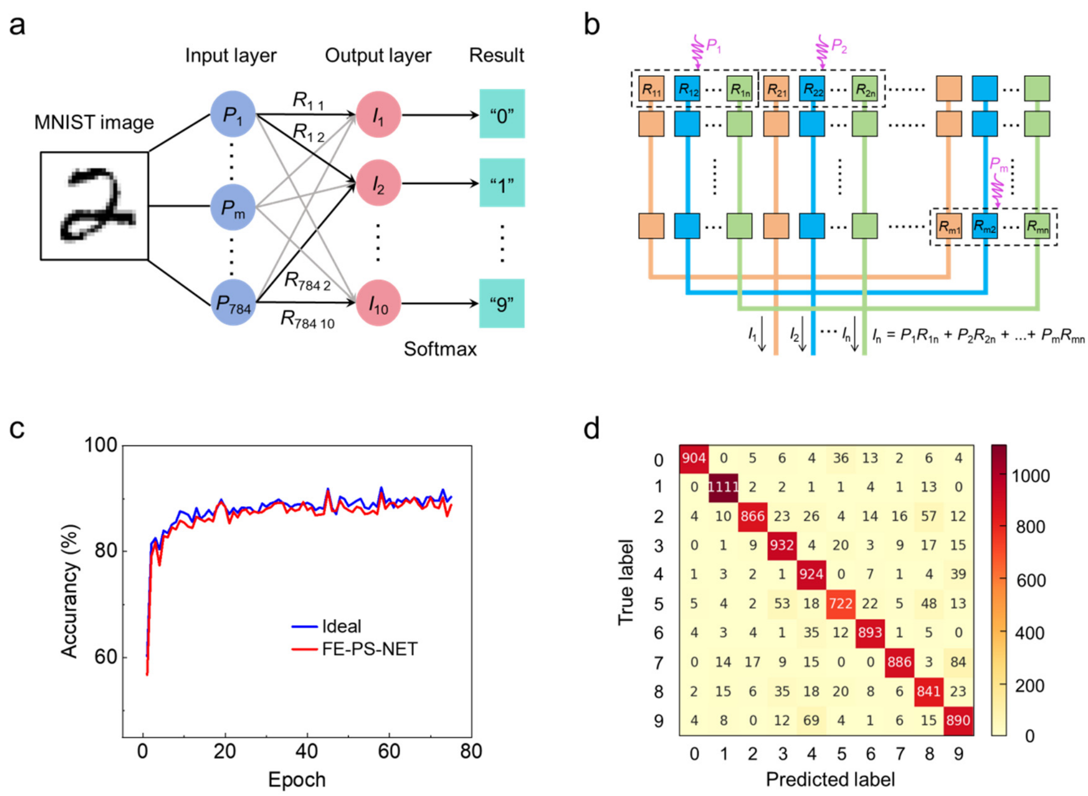

Figure S17. (a) Schematic illustration of the recognition of the MNIST handwritten digits based on a 784 × 10 ANN. (b) Implementation of the ANN on the FE-PS-NET, where each weight is mapped onto the photoresponsivity of the corresponding FE-PS. (c) Test accuracies of the simulated FE-PS-NET and an ideal floating-point-based ANN as a function of training epoch. (d) Confusion matrix after 75 training epochs.

To show the potential use of a large-scale FE-PS-NET with in situ training capability, a simulation of handwritten digit recognition using this large-scale FE-PS-NET is carried out. The handwritten digit images (28 × 28 pixels) are taken from the "Modified National Institute of Standards and Technology" (MNIST) dataset [http://yann.lecun.com/exdb/mnist/], which contain 60000 and 10000 images for training and test, respectively. To recognize these images, a 784 × 10 ANN is constructed (Fig.

S17a). This ANN can be implemented on the FE-PS-NET (Fig. S17b) by using photoresponsity to map weight. The FE-PS-NET consists of 784 pixels with each pixel divided into 10 subpixels (note: one subpixel corresponds to one FE-PS). The FE-PSs with the same subpixel index but different pixel indices are connected in parallel, and hence the output current along the *n*-th column is given by

$$I_n = \sum_{m=1}^{M} R_{mn} P_m \text{ , (S1)}$$

where R_{mn} is the of the FE-PS at the *m*-th pixel and *n*-th subpixel, P_m is the input optical power at the *m*-th pixel. During the training, a cross-entropy function is used as the loss function. In addition, the weight update of each FE-PS follows the experimental result under the BD-CL programming scheme.

As shown in Fig. S17c, the simulated FE-PS-NET achieves accuracies close to the ideal values during the training. Figure S17d further demonstrates that most of the digits are correctly recognized by the simulated FE-PS-NET after the training.

Table S1. Performance comparison between our FE-PS and other emerging programmable photosensors for in-sensor computing.

Device	I_{ph}-I_{light} relationship	Retention	Photoresponse time	Self-powered	Endurance	Write time	Write energy	No. of weights in LTP/LTD	C2C variation	D2D variation	Ref.
PZT-based FE-PS	Linear	15 days	30 μs	Yes	10^9	100 ns	1.77 nJ	21	0.66%	2.72%	This work
$MoTe_2$ /P(VDF-TrFE)-based homojunction	Linear	24 h	0.6-1.9 μs	Yes	10^6	50 μs	0.1 pJ	51	–	–	[4]
$CuInS_2P_6$-based photodiode	Nonlinear	3000 s	4 ms	Yes	10^5	100 ms	–	20	–	–	[5]
DIPAB/CuPc-based photomemristor	Linear	600 s	–	Yes	–	100 ms	1.87 nJ	~80	–	–	[6]
SWNT/GDY-based heterostructure	Linear	10^4 s	~5 ms	No	10^5	1 ms	50 aJ	32	–	–	[7]
WS_2-based nanotube	Linear	7-10 days	64-77 μs	Yes	–	5 μs	few hundred nJ	250	–	–	[8]
WSe_2/h-BN/Al_2O_3-based heterostructure	Nonlinear	–	4-8 ms	No	–	DC[a]	DC	–	–	–	[9]
Si_3N_4-based phototransistor	Linear	10^5 s	1 ms	No	–	DC	DC	32	–	–	[10]
Black phosphorous-based phototransistor	Linear	2000 s	–	No	200	20 ms	<2 μJ	36	–	< 8%	[11]
$Cs_2AgBiBr_6$-based photosensor	Linear	2000 s	–	Yes	500	500 ms	–	–	–	–	[12]
MoS_2-based MOS capacitor	–	10^3 min	–	No	10^6	1 μs	–	31	–	–	[13]
WSe_2-based photodiode	Linear	1000 s	40 ns	Yes	–	–	–	–	–	–	[14]
$PdSe_2$/$MoTe_2$-based heterostructure	Linear	–	0.4-4.5 μs	No	–	DC	DC	10	–	–	[15]
$MoS_{2-x}O_x$-based photomemristor	–	3000 s	1.38-3.8 ms	Yes	100	–	–	–	–	–	[16]
MoS_2-based photodiode	Linear	1000 s	–	Yes	–	100 ms	–	168	–	–	[17]
DIPAB/CuPc-based photomemristor	Nonlinear	3000 s	–	No	2000	400 ms	0.1-37.8 nJ	12	–	–	[18]
WSe_2/h-BN/MoS_2-based phototransistor	Linear	–	500 ns	No	–	DC	DC	11	–	–	[19]
WS_2/DIPAB-based photomemristor	Linear	10^4 s	–	Yes	–	400 ms	–	40	–	–	[20]
NbS_2/MoS_2-based phototransistor	Nonlinear	1000 s	304 ms	No	–	DC	DC	15	–	3%	[21]

[a] "DC" refers to that DC gate voltages are used for the weight writing.

References

1. Tan, Z. et al. Thinning ferroelectric films for high-efficiency photovoltaics based on the Schottky barrier effect. *NPG Asia Mater.* **11**, 20 (2019).

2. Cui, B. et al. Ferroelectric photosensor network: an advanced hardware solution to real-time machine vision. *Nat. Commun.* **13**, 1707 (2022).

3. Li, W. et al. Polarization-dominated internal timing mechanism in a ferroelectric second-order memristor. *Phys. Rev. Appl.* **19**, 014054 (2023).

4. Wu, G. et al. Ferroelectric-defined reconfigurable homojunctions for in-memory sensing and computing. *Nat. Mater.* **22**, 1499-1506 (2023).

5. Wang, Y. et al. A three-dimensional neuromorphic photosensor array for nonvolatile in-sensor computing. *Nano Lett.* **23**, 10 (2023).

6. Cai, Y. et al. In-situ artificial retina with all-in-one reconfigurable photomemristor networks. *npj Flex. Electron*. **7**, 29 (2023).

7. Zhang, G. et al. Broadband sensory networks with locally stored responsivities for neuromorphic machine vision. *Sci. Adv*. **9**, eadi5104 (2023).

8. Sun, Y. et al. Mesoscopic sliding ferroelectricity enabled photovoltaic random access memory for material-level artificial vision system. Nat. Commun. 13, 5391 (2022).

9. Wang, C. et al. Gate-tunable van der Waals heterostructure for reconfigurable neural network vision sensor. *Sci. Adv.* **6**, eaba6173 (2020).

10. Han, JK. et al. Mnemonic-opto-synaptic transistor for in-sensor vision system. *Sci. Rep.* **12**, 1818 (2022).

11. Lee, S., Peng, R., Wu, C. & Li, M. Programmable black phosphorus image sensor for broadband optoelectronic edge computing. *Nat. Commun.* **13**, 1485 (2022).

12. Dun, G. et al. Reconfigurable Pb-Free perovskite array for X-ray in-sensor computing. *IEEE Trans. Electron Devices* **70**, 2147-2152 (2023).

13. Kumar, D., Joharji, L., Li, H., Rezk, A., Nayfeh, A. & El-Atab, N. Artificial visual perception neural system using a solution-processable MoS_2-based in-memory light sensor. *Light Sci. Appl.* **12**, 109 (2023).

14. Mennel, L., Symonowicz, J., Wachter, S., Polyushkin, D., Molina-Mendoza, A.J. & Mueller, T. Ultrafast machine vision with 2D material neural network image sensors. *Nature* **579**, 62-66 (2020).

15. Pi, L. et al. Broadband convolutional processing using band-alignment-tunable heterostructures. *Nat. Electron.* **5**, 248-254 (2022).

16. Fu, X. et al. Graphene/$MoS_{2-x}O_x$/graphene photomemristor with tunable non-volatile responsivities for neuromorphic vision processing. *Light Sci. Appl.* **12**, 39 (2023).

17. Li, T. et al. Reconfigurable, non-volatile neuromorphic photovoltaics. Nat. Nanotechnol. 18, 1303-1310 (2023).

18. Cai, Y. et al. Molecular ferroelectric/semiconductor interfacial memristors for artificial synapses. *npj Flex Electron* **6**, 16 (2022).

19. Zhang, T. et al. High performance artificial visual perception and recognition with a plasmon-enhanced 2D material neural network. *Nat. Commun.* **15**, 2471 (2024).

20. Cai, Y. et al. In-plane ferroelectric-reconfigured interface towards dual-modal intelligent vision. *Next Nanotechnology* **5**, 100052 (2024).

21. Huang, P. et al. Neuro-inspired optical sensor array for high-accuracy static image recognition and dynamic trace extraction. Nat. Commun. 14, 6736 (2023).